HiLL PUBLISHING

Journal of Applied Mathematics and Computation, 2024, 8(4), 319-324
https://www.hillpublisher.com/journals/JAMC/
ISSN Online: 2576-0653
ISSN Print: 2576-0645

The Characteristics of Two-phase Flow in Porous Media over Wide Range of Capillary, Viscous, and Inertial Force

Kailin Wang, Shintaro Matsushita*, Sotheavuth Sin, Wilson Susanto, Bowen Wang, Tetsuya Suekane

Department of Mechanical Engineering, Institute of Science Tokyo, 2-12-1-I6-33, Ookayama, Meguro-ku, Tokyo 152-8550, Japan.

How to cite this paper: Kailin Wang, Shintaro Matsushita, Sotheavuth Sin, Wilson Susanto, Bowen Wang, Tetsuya Suekane. (2024) The Characteristics of Two-phase Flow in Porous Media over Wide Range of Capillary, Viscous, and Inertial Force. *Journal of Applied Mathematics and Computation*, 8(4), 319-324.
DOI: 10.26855/jamc.2024.12.006

Received: November 25, 2024
Accepted: December 23, 2024
Published: January 20, 2025

***Corresponding author:** Shintaro Matsushita, Department of Mechanical Engineering, Institute of Science Tokyo, 2-12-1-I6-33, Ookayama, Meguro-ku, Tokyo 152-8550, Japan.

Abstract

The characteristic of two-phase immiscible flow in porous media is controlled by different kinds of force, such as interface surface tension (capillary force) and fluid viscosity (viscous force). Based on those two forces, three typical displacement patterns in porous media are divided, named as capillary fingering, viscous fingering and stable displacement. However, the impact of inertial force in displacement pattern, which generate due to the flow direction or velocity change of fluid, is always neglected. This research used direct numerical simulation (DNS) to study the two-phase immiscible pattern with a wide range of capillary number (*Ca*) and ratio of Reynolds number (*Re*). The *Ca* is a dimensionless value which represents the ratio of viscous force and capillary force. While *Re* represents the ratio of inertial force and viscous force. The impact of forces on displacement patterns were determined based on the quantitative analyses of the saturation distribution as functions of *Ca* and *Re*. The result shows that inertial effects have minimal influence on flow conditions at low capillary numbers. However, at high capillary numbers, capillary forces become less significant, and inertial effects strongly influence flow conditions. These findings contribute the different insight of fluid displacement patterns, controlled by balance of inertial, capillary and viscous forces, has a noticeable influence on recovery or storage efficiency in subsurface process.

Keywords

Porous media; fluid dynamic simulation; weakly compressible scheme; phase filed method; surface energy; capillary fingering; viscous fingering

1. Introduction

Multiple immiscible flows in porous media are ubiquitous phenomena in both natural and industrial settings [1-4]. These processes play crucial roles in various fields, including environmental science, the oil industry, hydrogeology, and even modern fuel cell technology. The physics governing these flows apply across a wide range of scales, from tiny catalyst pores to vast underground reservoirs. In environmental science, for instance, these principles are applied in carbon capture and storage, where CO_2 is injected into porous rock formations. The oil industry utilizes similar concepts for enhanced oil recovery (EOR). Hydrogeologists employ these principles to study groundwater movement and contaminant transport. Even modern fuel cells rely on managing different fluids through porous materials. Industrial processes such as drying and chemical reactions also rely on the understanding of multiphase flows in porous media. The widespread importance of this phenomenon across diverse areas underscores the need for thorough research and modelling.

Previous studies have shown that fingering flows in drainage processes depend on the balance between capillary and

viscous forces. Two key dimensionless numbers guide our understanding: the capillary number (*Ca*) and the viscosity ratio (*M*). *Ca* represents the ratio of viscous to capillary forces, defined as

$$Ca = \frac{\mu q}{\sigma}. \tag{1}$$

where μ is the viscosity of the injected phase, q is the darcy velocity of the injected phase, σ is the interfacial tension. While M is the viscosity ratio between invading and defending fluids, defined as

$$M = \frac{\mu_i}{\mu_d}. \tag{2}$$

where $\boldsymbol{\mu_i}$ is the viscosity of the invading phase, $\boldsymbol{\mu_d}$ is the viscosity of the defending phase.

Hu et al [5]. used these numbers to classify displacement patterns into three types: stable displacement, capillary fingering, and viscous fingering. Stable displacement shows a compact structure with high saturation. Here, the invading phase uniformly pushes out the defending phase, resulting in almost complete displacement. Viscous fingering, in contrast, forms thin finger structures along preferred flow paths. These fingers move rapidly in the injection direction without backward movement. Due to this quick breakthrough, viscous fingering typically results in lower saturation than the other two patterns. Capillary fingering produces plump finger structures. In this pattern, the invading phase tends to occupy larger throat sizes compared to viscous fingering [6]. This characteristic contributes to a higher saturation than the viscous fingering. However, other factors also influence the flow process, including density, surface wettability, and pore size distribution. Recent studies have highlighted the impact of inertial forces on porous media flow, though many limitations remain [7]. In our current research, we focus on how changes in density affect these inertial effects.

By nondimensionalizing the momentum equation, we can find three important dimensionless quantities: the Reynolds number (*Re*), viscosity ratio (*M*), and Weber number (*We*). The Reynolds number compares inertial forces to viscous forces, defined as

$$Re = \frac{\rho u L}{\mu}. \tag{3}$$

where ρ is the density of the fluid, u is the flow speed, L is the characteristic length, μ is the dynamic viscosity of the fluid. While the Weber number relates inertial forces to surface tension, defined as

$$We = \frac{\rho L u^2}{\mu}. \tag{4}$$

Interestingly, the capillary number can be derived as the ratio of the Weber number to the Reynolds number, that is,

$$Ca = \frac{We}{Re} = \frac{\mu u}{\sigma}. \tag{5}$$

This relationship led us to consider another important dimensionless quantity: the Reynolds number ratio, defined as

$$R = \frac{Re_d}{Re_i} = \frac{\rho_d \mu_i}{\rho_i \mu_d}. \tag{6}$$

This ratio incorporates both viscosity and density ratios, offering a more comprehensive view of fluid interactions.

Our current research aims to investigate how inertial effects influence flow characteristics in porous media. Specifically, we study two fluids with the same viscosity but different densities, allowing us to isolate the impact of the Reynolds ratio. Using the direct numerical method proposed in previous studies [8-10], we conduct a numerical study of two-phase flow characteristics in porous media, examining various capillary numbers and Reynolds number ratios.

2. Numerical Method

2.1 Fluid dynamic equations

The conservation of mass, momentum conservation of Navier-stokes equation, and weekly compressible constraint under isothermal condition can be expressed as

$$\frac{\partial \rho}{\partial t} + \nabla \cdot (\rho \boldsymbol{u}) = 0, \tag{7}$$

$$\frac{\partial \rho \boldsymbol{u}}{\partial t} + \nabla \cdot (\rho \boldsymbol{u} \otimes \boldsymbol{u}) = -\nabla p + \nabla \cdot \boldsymbol{\tau} + \boldsymbol{F}, \tag{8}$$

$$\frac{\partial p}{\partial t} = -\rho c_s^2 \nabla \cdot \boldsymbol{u} \tag{9}$$

where the velocity vector $\boldsymbol{u}$= ($\boldsymbol{u}$, $\boldsymbol{v}$, $\boldsymbol{w}$), the viscous stress tensor $\boldsymbol{\tau} = \mu(\nabla \boldsymbol{u} + \nabla \boldsymbol{u}^T)$. ρ, p and μ are the density, pressure and

dynamic viscous coefficient, respectively. F is the external body forces terms such as influences of surface tension and gravity. c_s is the artificial velocity of sound. A common criterion is that the fluid can be regarded as incompressible when the density change is lower than 5%. Since we don't want to consider the effect of the fluid's compressibility, we will keep the Mach number below 0.03 to maintain low compressibility.

In this study, an evolving pressure projection method [10] is used to solve Navier-Stokes equations. It can transmit the pressure change anywhere throughout fluid immediately and reduce the negative effect of the acoustic wave to ensure the accuracy of the velocity and pressure fields. It should be mentioned that this method also helps to reduce fluid compressibility in our simulation.

2.2 Interface capturing method

We consider a whole-domain description which simulates a two-phase immiscible fluid system as single-fluid model. A fluid field function Φ is used to describe the phase distribution in the system, and the motion of the interface between different fluids is solved by the conservative phase-field equation [8] coupled with level-set method.

$$\frac{\partial \emptyset}{\partial t} + \nabla \cdot (\boldsymbol{u}\emptyset) = \nabla \cdot \left[M\left(\nabla\emptyset - \frac{4\emptyset(1-\emptyset)}{W}\boldsymbol{n}\right)\right], \tag{10}$$

where M and W are the mobility and the thickness of interface, respectively. n is the outward-normal vector of each interface unit. Φ is the phase field function changing from 0 to 1 based on the fraction between different phase of fluid which are defined as:

$$\emptyset(\boldsymbol{x}, t) = \begin{cases} 0, & light\ fluid \\ 0{\sim}1, & interface \\ 1, & heavy\ fluid. \end{cases} \tag{11}$$

where the subscript 'l' and 'h' are indicated on light and heavy fluid, respectively.

Due to the good geometric description for interface, the level-set function ψ is introduced to calculate the normal vector and the curvature of interface with high accuracy, and it also used for surface tension force and contact angle calculation in our simulation. Time evolution of level-set function ψ follows the advection equation:

$$\frac{\partial \psi}{\partial t} = -(\boldsymbol{u} \cdot \nabla)\psi. \tag{12}$$

The external force terms F in Eq. (8) typically consists of two parts, the surface tension Fs part and gravity part $F_g = \rho g$. In our study, a density-scaled balance CSF (continuum surface force) model [8] is applied to calculate the surface tension force. This model has a good performance that can minimize spurious current (*e.g.*, balance velocity fields near the fluid-fluid interface).

$$\boldsymbol{F_s} = \frac{2\rho}{\rho_l + \rho_h}\sigma\kappa\nabla\emptyset \tag{13}$$

where σ is the surface tension coefficient and κ is the interface curvature of two liquid. The normal vector n in Eq. (10) and the interface curvature κ are calculated by the level-set function:

$$\boldsymbol{n} = \frac{\nabla\psi}{|\nabla\psi|} \tag{14}$$

$$\kappa = -\nabla \cdot \left(\frac{\nabla\psi}{|\nabla\psi|}\right) \tag{15}$$

3. Results and Discussion

In our simulations, we explored a range of capillary numbers and Reynolds ratios. Figure 1 shows the fluid distributions at breakthrough time for these different conditions. These results provide a visual representation of how changing capillary numbers and Reynolds ratios affect flow patterns.

3.1 Low capillary number conditions

At low capillary numbers ($logCa$ = -4), our simulations reveal that the flow pattern hardly changes with the Reynolds ratio, as shown in Figure 1 (Blue: invading phase; Yellow: defending phase; Black: solid). This observation is further supported by the cross-sectional saturation at the breakthrough time presented in Figure 2. The saturation, calculated as the ratio of fluid nodes occupied by the invading fluid to the total fluid nodes, remains relatively constant across different Reynolds ratios. The dashed lines of the same color in the figure are trend lines.

These results indicate that at low capillary numbers, capillary forces dominate, while the effects of viscous and inertial forces are relatively not important. Besides, we can also find that the saturation at each cross-section is almost above 40%, and the flow shows the characteristics of capillary fingering.

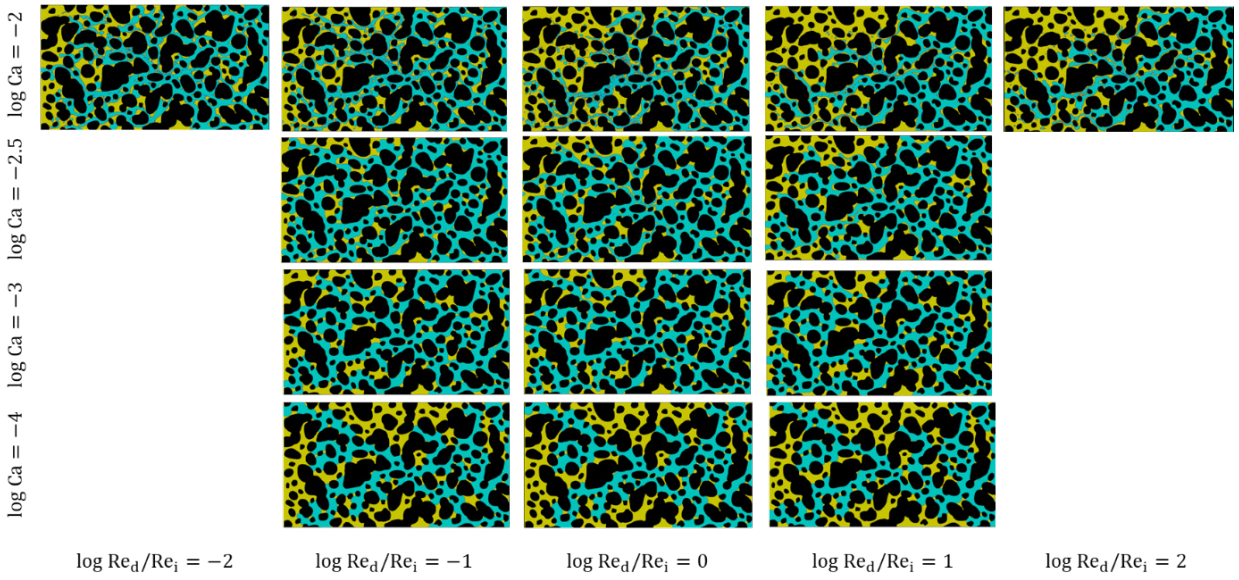

Figure 1. Fluid distributions at the breakthrough time.

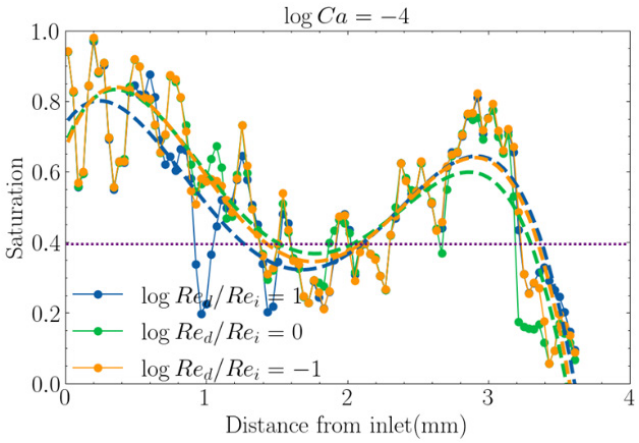

Figure 2. Cross-sectional saturation at low Capillary numbers.

3.2 High capillary number conditions

Under high capillary number conditions ($logCa$ = -2), the flow pattern changes with variations in the Reynolds ratio. In these conditions, capillary forces become less important, and the interplay between viscous and inertial forces dominates. At high Reynolds ratio ($logRe_d/Re_i$ = 1, 2), Reynolds ratio

$$R = \frac{Re_d}{Re_i} = \frac{\rho_d \mu_i}{\rho_i \mu_d} > 1. \tag{16}$$

And since $\mu_i = \mu_d$, we can get $\rho_d > \rho_i$. In this case, the inertial force of the defending phase exerts a greater influence on the flow. As shown in Figure 3, the saturation is higher near the inlet and very low near the outlet. The flow exhibits characteristics of stable displacement near the inlet and viscous fingering near the outlet. Conversely, at low Reynolds ratios ($logRe_d/Re_i$ = -1, -2), Reynolds ratio $R < 1$, we can get $\rho_d < \rho_i$. In this case, the inertial force of the invading phase has a more pronounced effect. As shown in Figure 3, there is high saturation near both the inlet and outlet, with slightly lower saturation near the inlet compared to the high Reynolds ratio cases. The flow pattern shows stable displacement characteristics near the inlet and viscous fingering near the outlet.

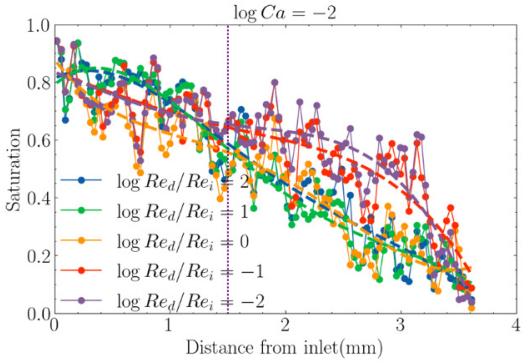

Figure 3. Cross-sectional saturation at high Capillary numbers.

When the two fluids have the same Reynolds number ($logRe_d/Re_i = 0$), we observe a transition state between the two patterns mentioned above. The flow characteristics near the inlet resemble those of the low Reynolds ratio case, while near the outlet, they are similar to the high Reynolds ratio case.

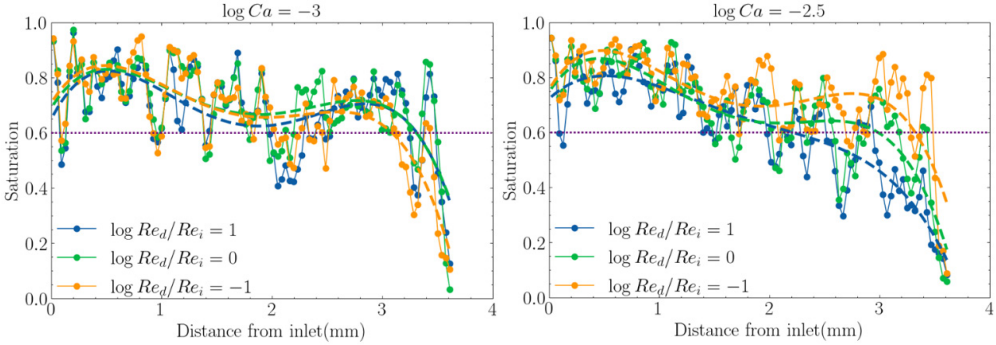

Figure 4. Cross-sectional saturation at intermediate capillary numbers.

3.3 Intermediate capillary number conditions

For intermediate capillary numbers ($logCa$ = -3, -2.5), the flow pattern changes slightly with variations in the Reynolds ratio. As illustrated in Figure 4, the saturation at each cross-section is mostly above 60%. And the flow shows the characteristics of stable displacement.

3.4 Overall saturation trend analysis

Figure 5 presents the overall saturation trends observed in our simulations. At fixed, relatively low capillary numbers, the saturation remains constant with changes in the Reynolds ratio. However, at higher capillary numbers, the saturation varies with the Reynolds ratio, with higher saturation observed at low Reynolds ratios. This is similar to the previous conclusion that capillary forces have a greater impact at low capillary numbers, while capillary forces are no longer important at high capillary numbers.

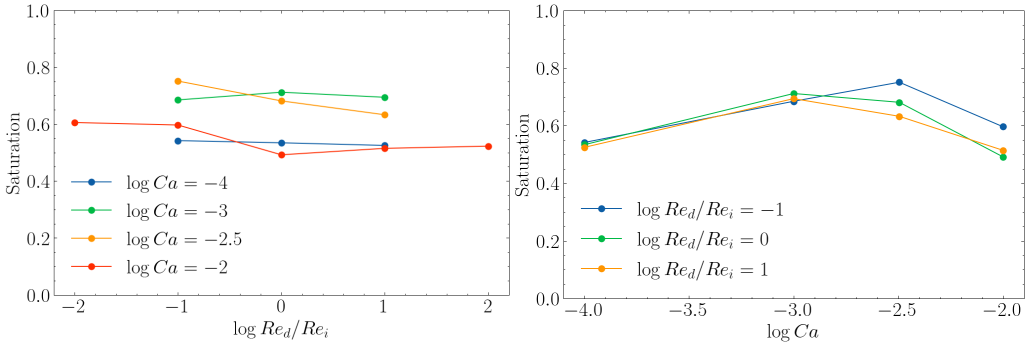

Figure 5. Overall saturation trend.

When the Reynolds ratio is fixed, the saturation first increases and then decreases as the capillary number increases. We hypothesize that this non-monotonic behavior may be due to the formation of vortices in the flow field at high capillary numbers, resulting from high flow velocities and Reynolds numbers.

4. Conclusion

Our research provides valuable insights into the complex interplay between capillary forces, viscous forces, and inertial effects in two-phase flows through porous media. We found that:

(1) At low capillary numbers, inertial effects have minimal influence on flow conditions, and capillary forces dominate.

(2) At high capillary numbers, capillary forces become less significant, and inertial effects strongly influence flow conditions.

(i) When the invading phase density is greater (low Reynolds ratio), the inertial effect of the invading phase has a greater influence, and the flow distribution approaches stable displacement.

(ii) When the invading phase density is smaller (high Reynolds ratio), the inertial effect of the defending phase has a greater influence, resulting in stable displacement near the inlet and viscous fingering near the outlet.

These findings contribute to our understanding of multiphase flows in porous media and have potential implications for various applications, including enhanced oil recovery, carbon sequestration, and groundwater remediation.

Acknowledgements

The authors acknowledge the fellowship support from the China Scholarship Council (Student ID: 202006280051) for study at the Institute of Science Tokyo. This study was also supported by the Japan Society for the Promotion of Science KAKENHI (grant numbers: 22H03770 and 22K14178). The authors thank the Institute of Science Tokyo for the use of the computing resources of the TSUBAME 4.0 supercomputer.

References

[1] Wang K, Li L, Wang Y, Zhang S. Design and hydraulic performance studies on an axial lead-bismuth pump for GEN-IV reactors. Int. J. Energy Res. 2021;45:11822-11836. https://doi.org/10.1002/er.5778.

[2] Li X, Li L, Ma W, Wang W. Two-phase flow patterns identification in porous media using feature extraction and SVM. Int. J. Multiph. Flow. 2022;156:104222. https://doi.org/10.1016/j.ijmultiphaseflow.2022.104222.

[3] Sin S, Imai S, Mahardika MA, Patmonoaji A, Nasir M, Susanto W, Matsushita S, Suekane T. Three-dimensional visualization of Rayleigh-Bénard convection in porous media. Adv. Water Resour. 2024;186:104666. https://doi.org/10.1016/j.advwatres.2024.104666.

[4] Xu H, Liu Y, He S, Zheng JN, Jiang L, Song Y. Enhanced CO2 hydrate formation using hydrogen-rich stones, L-Methionine and SDS: Insights from kinetic and morphological studies. Energy. 2024;291:130280. https://doi.org/10.1016/j.energy.2024.130280.

[5] Hu Y, Patmonoaji A, Zhang C, Suekane T. Experimental study on the displacement patterns and the phase diagram of immiscible fluid displacement in three-dimensional porous media. Adv. Water Resour. 2020;140:103584. https://doi.org/10.1016/j.advwatres.2020.103584.

[6] Mo J, Zhang C, Zheng W, Hu Y, Li Z, Suekane T. Influence of binder content on gas-water two-phase flow and displacement phase diagram in the gas diffusion layer of PEMFC: A pore network view. Int. J. Heat Mass Transf. 2024;231:125838. https://doi.org/10.1016/j.ijheatmasstransfer.2024.125838.

[7] Wang K, Matsushita S, Yamashita S, Nasir M, Suekane T. Energy transfer process during Haines jumps and meniscus reconfiguration with a high-density and viscosity ratio. Int. J. Heat Mass Transf. 2024;230:125749. https://doi.org/10.1016/j.ijheatmasstransfer.2024.125749.

[8] Matsushita S, Aoki T. A weakly compressible scheme with a diffuse-interface method for low Mach number two-phase flows. J. Comput. Phys. 2019;376:838-862. https://doi.org/10.1016/j.jcp.2018.10.019.

[9] Matsushita S, Aoki T. Gas-liquid two-phase flows simulation based on weakly compressible scheme with interface-adapted AMR method. J. Comput. Phys. 2021;445:110605. https://doi.org/10.1016/j.jcp.2021.110605.

[10] Yang K, Aoki T. Weakly compressible Navier-Stokes solver based on evolving pressure projection method for two-phase flow simulations. J. Comput. Phys. 2021;431:110113. https://doi.org/10.1016/j.jcp.2021.110113.